Inverse Opal Photonic Nanostructures for Enhanced Light Harvesting in CH3NH3PbI3 Perovskite Solar Cells

Daem, Nathan ; Mayer, Alexandre; Spronck, Gilles ; Colson, Pierre ; Loicq, J.J.D.; Henrist, Catherine ; Cloots, Rudi ; Maho, Anthony ; Lobet, Michael

DOI
10.1021/acsanm.2c03274

Publication date
2022

Document Version
Final published version

Published in
ACS Applied Nano Materials

ACS APPLIED NANO MATERIALS

www.acsanm.org Article

Inverse Opal Photonic Nanostructures for Enhanced Light Harvesting in $CH_3NH_3PbI_3$ Perovskite Solar Cells

Nathan Daem, Alexandre Mayer, Gilles Spronck, Pierre Colson, Jerôme Loicq, Catherine Henrist, Rudi Cloots, Anthony Maho, Michaël Lobet, and Jennifer Dewalque*

Cite This: *ACS Appl. Nano Mater.* 2022, 5, 13583−13593 Read Online

ACCESS | Metrics & More | Article Recommendations | Supporting Information

ABSTRACT: Light management strategies using photonic crystals have been proven to efficiently improve light harvesting and subsequently conversion efficiency of various optoelectronic devices. This study focuses on 3D inverse opal $CH_3NH_3PbI_3$ photoanodes in perovskite solar cells from a combined numerical and experimental approach. Varying the pore size and the layer thickness in numerical simulations, we first determined theoretical optimum from a purely optical point of view. Corresponding 3D inverse opal photonic nanostructures were then fabricated through spin-coating protocols using polystyrene nanospheres of various diameters as hard templating sacrificial agents. It demonstrates how the photonic nanostructuration of the perovskite layer impacts both optical and electronic properties of experimental samples. Regarding the individual 3D inverse opal perovskite layers, an optimum of light absorption is reached for an ∼500 nm diameter pore photonic nanostructure, with a photonic absorption enhancement as high as 16.1% compared to an unstructured compact benchmark. However, in addition to electronic-related countereffects, local light absorption in the hole transporting material is observed in assembled solar cells, weakening the light management benefits of the perovskite layer nanostructuration to only ∼3% photonic enhancement.

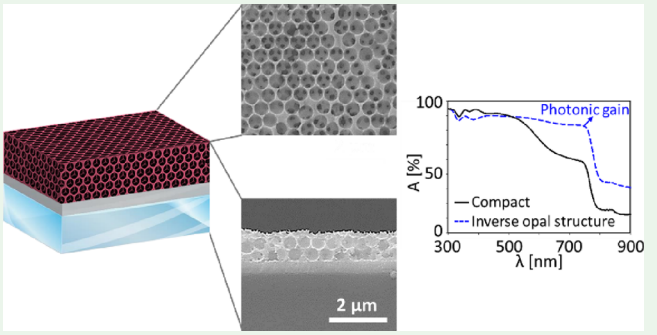

KEYWORDS: *$CH_3NH_3PbI_3$ perovskite, photonic crystals, 3D inverse opal nanostructuration, light management, solar cells, genetic algorithm*

1. INTRODUCTION

In the past decade, organolead halide perovskite solar cells (PSCs) have attracted increasing attention owing to their power conversion efficiency (PCE) rising over 25%, making them serious alternatives to widely used silicon solar cells and thin film-based technologies.[1]

These perovskite-based materials present tremendous technological advantages such as low-cost solution processing, color tunability, and device flexibility, allowing them to meet the main requirements for designing novel portable and/or aesthetic applications. The latter range from building integrated photovoltaics (BIPV) solutions, autonomous power supply for wearable electronics (phones, tablets, watches, sensors, etc.), smart decorative accessories to textiles.

$CH_3NH_3PbI_3$—also referred to as $MAPbI_3$ (CH_3NH_3 = methyl ammonium (MA))—is the archetypical reference compound of the organolead halide perovskite materials family.[2−4] The $MAPbI_3$ formulation is at the origin of the outstanding research on PSCs, initiated by Kojima *et al.* in 2009.[5] The large absorption coefficient of the organolead halide perovskite photoabsorbers allows light to be absorbed by a thin layer, generally in the thickness range of 300−600 nm.[4,6] To further improve light harvesting, special attention has been paid over the recent years to enhance light−matter interactions and consequently the electric field intensity within the perovskite photoactive materials.[7−9]

Among different light management strategies, anti-reflective coatings,[10−12] textured surfaces,[13,14] plasmonic,[15−17] or light scattering layers[18] are used in photovoltaic devices. Photonic crystals (PCs) have also attracted particular attention because of their unique ability to mold the flow of light.[19−22] The photonic band structure allows to control light collection and emission of the devices, notably through photonic band gaps or quasi-guided mode excitation presenting a Fano resonance lineshape.[7,23−26] In the case of $MAPbI_3$-based PSCs, enhancing light harvesting efficiency in the long-wavelength range is particularly important because light absorption of $MAPbI_3$ typically decreases between 500 and 800 nm.[27,28]

Received: July 26, 2022
Accepted: September 5, 2022
Published: September 15, 2022

The photonic structuration in PSCs has been investigated with different dimensionalities (1D, 2D, or 3D), with the aim to increase the photocurrent generation and the PCE. For example, Ramos *et al.*[29] observed enhanced photocurrent using 1D-PCs layered photoanodes prepared from an angle physical deposition process (PVD-OAD). In the case of 2D- and 3D-PCs, periodic structurations at the nanoscale of the porous TiO_2 electron transporting layer (ETL) or of the perovskite photoactive layer notably include a honeycomb structure, moth-eye structure, or inverse opal (IO), prepared from nanosphere lithography,[30−33] nanoimprinting,[34] or derived templating techniques based on 3D self-assembly of solid spheres[35−38] or microgels.[39] Correlation between light absorption enhancement and device PCE improvement is well established for photonically nanostructured TiO_2 photoelectrodes through theoretical simulations[40−42] and experimental works.[35,43,44] Numerical simulations performed by a finite-difference time-domain (FDTD) method or rigorous coupled-wave analysis (RCWA) also highlight the positive impact of 2D-PCs perovskite layers in terms of light absorption enhancement for cylindrical nanoholes[45,46] or inverted vertical cone nanostructures.[47] However, a few experimental works tackle the photonic structuration of the perovskite layers and only 2D-IO arrangements are considered.[32,33] These studies showed PCE improvement through 2D-IO structuration of the perovskite layer, without specific investigation of the photonic effects and quantitative analysis of the light absorption gain.

In this paper, we focused on 3D-IO $MAPbI_3$ perovskite photoanodes. To the best of our knowledge, 3D-IO photonic structuration of the perovskite photoactive layer has never been reported for specific use in PSCs. Tüysüz's group successfully prepared 3D-IO lead halide perovskite for laser (but not for PV) applications, highlighting photonic enhancement of experimentally processed samples.[36−38]

The purpose of this study is therefore to evidence the potential benefits of the 3D-IO photonic structuration of the perovskite photoactive layer in terms of light harvesting on the one hand and in terms of charge generation and collection in PSCs on the other hand. Our first goal is to assess how an optimal photonic nanostructuration of the perovskite layer—determined from numerical simulation—impacts both optical and electronic properties of experimental samples. The control of the PCs dimensions, especially the pore size in 3D-IO nanostructures, is of utmost importance to enhance light harvesting toward the excitation of quasi-guided modes close to the electronic band gap.[35,40,41] Therefore, from a purely optical point of view, light harvesting and global absorptance have been assessed with numerical simulations. The aim is to find the best performing 3D-IO photonic nanostructure in terms of pore size and layer thickness.

We then implemented the obtained 3D-IO optimum, first as individual 3D-IO nanostructured $MAPbI_3$ perovskite layers and further as assembled devices. The morphological, structural, optical, and electronic properties of the experimentally processed samples were characterized and discussed in light of the simulated results. In comparison with an unstructured compact perovskite layer counterpart, we aimed to discriminate light harvesting modulation and charge transfer property modification induced by the 3D-IO photonic nanostructuration of the perovskite photoactive layer. Especially, the PCE of the assembled devices was investigated.

This work is the first to evidence the best 3D-IO photonic nanostructure for $MAPbI_3$-based PSCs from a combined numerical and experimental approach.

2. RESULTS AND DISCUSSION

2.1. Inverse Opal $MAPbI_3$ Photonic Nanostructure and Optimum Design Methodology. Figure 1 shows the 3D-IO photonic nanostructure under investigation and integrated in the full PSC stack.

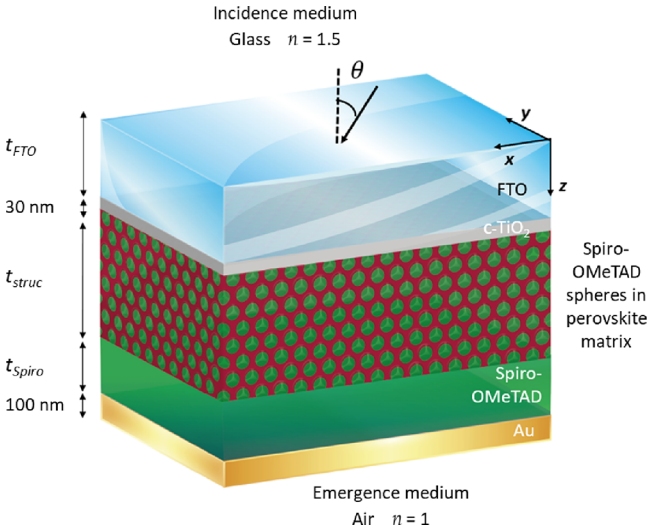

Figure 1. 3D inverse opal $MAPbI_3$ photonic nanostructure.

In our numerical simulations, the incidence medium is a semi-infinite non-dispersive uniform glass material that is covered by a uniform fluorine-doped tin oxide (FTO) transparent conducting layer and a dense TiO_2 layer (c-TiO_2). The specific case of the air/glass interface occurring in a real device is treated independently and mathematically below. The photoactive layer is a 3D-IO photonically nanostructured $MAPbI_3$ perovskite layer in comparison with an unstructured compact $MAPbI_3$ reference. The 3D-IO $MAPbI_3$ perovskite layer is further filled by Spiro-OMeTAD hole transporting material (HTM). The resulting 3D-IO photonic nanostructure then consists of N layers (N = 1, 2, and 3) of Spiro-OMeTAD HTM spheres of diameter D embedded in a $MAPbI_3$ perovskite host matrix. In our model, the spheres are arranged according to a face-centered cubic (fcc) close-packed structure, as expected from the literature.[36,38,48,49] A uniform Spiro-OMeTAD HTM overlayer is inserted between the 3D-IO nanostructured $MAPbI_3$ perovskite layer and the gold counter electrode. The latter also acts as a back reflector.

The optimal nanostructures are determined with the use of a home-made genetic algorithm (GA) in combination with a home-made RCWA method.[50,51] The light absorption enhancement is the figure of merit used to optimize the configuration. The RCWA method provides the numerical modeling of the considered optical systems.[52,53] More particularly, it enables to compute reflectance $R(\lambda)$ and transmittance $T(\lambda)$, from which global absorbance of the system $A(\lambda)$ can be deduced invoquing energy conservation. The critical parameter for numerical convergence is the number of plane waves along the x and y directions, which is set to 7 × 7. To reproduce the thick glass top layer (2.2 mm), the absorptance retrieved by RCWA A_{RCWA} must be

https://doi.org/10.1021/acsanm.2c03274
ACS Appl. Nano Mater. 2022, 5, 13583−13593

corrected by the transmittance $T_{air/glass}$ of the air/glass interface, such as $A(\lambda) = T_{air/glass} \times A_{RCWA}$ with $T_{air/glass} = 4n_{air}n_{glass}/|n_{air} + n_{glass}|^2$. The refractive index of air (n_{air}) is set equal to 1, while the dispersive refractive indices of glass (n_{glass}), FTO, TiO_2, Spiro-OMeTAD, and gold come from the literature.[54−56] The refractive index of $MAPbI_3$ perovskite was determined by ellipsometric measurement on a compact perovskite film deposited by spin-coating on a silicon substrate (Figure S1, Supporting Information).

From $A(\lambda)$, we are able to derive the theoretical photon-absorption efficiency η as a function of the geometrical parameters of the system.[40,50,51,53] This theoretical efficiency represents the fraction of incident photons that are absorbed in the device. It is the quantity (also referred to as the fitness) to be maximized by the genetic algorithm, assuming that each photon generates one electron−hole pair and increases in a way the integrated photon efficiency without losses. It reads

$$\eta = \frac{\int_{\lambda_{min}}^{\lambda_{max}} \frac{\lambda}{hc} S(\lambda)A(\lambda)d\lambda}{\int_{\lambda_{min}}^{\lambda_{max}} \frac{\lambda}{hc} S(\lambda)d\lambda} \quad (1)$$

with h being the Planck constant, c the speed of light in vacuum, $A(\lambda)$ the absorptance, $S(\lambda)$ the incident solar spectrum (AM1.5G), and λ_{min}= 310 nm and λ_{max} = 843 nm corresponding, respectively, to the lower bound of the solar spectrum and to the perovskite band gap determined experimentally. The genetic algorithm is responsible for the exploration of these parameters and provides ideally a globally optimal set of parameters for which the theoretical photon-absorption efficiency is maximal.

2.2. Numerical Simulations of the Microstructural Features for Optimal 3D-IO Nanostructured $MAPbI_3$ Photoanodes. We used the genetic algorithm to determine optimal parameters for (i) the thickness of the 3D-IO nanostructured $MAPbI_3$ perovskite layer, (ii) the diameter of the spheres of Spiro-OMeTAD, (iii) the thickness of the Spiro-OMeTAD overlayer, and (iv) the thickness of the FTO layer (Figure 1). The range of variations of these parameters and the optimal values found by the genetic algorithm are given in Table 1. The theoretical photon-absorption efficiency obtained with these optimal parameters is 92.1%. It should be noted here that the thicker FTO would artificially increase η via increased parasitic absorption, while the thinner Spiro-OMeTAD overlayer would not act as an efficient HTM anymore.[57,58]

Table 1. Parameters Determined by the Genetic Algorithm[a]

	x_{min} (nm)	x_{max} (nm)	x_{opt} (nm)
thickness of the 3D-IO $MAPbI_3$ layer	100	2200	1810
Spiro-OMeTAD sphere diameter	100	2200	560
thickness of the Spiro-OMeTAD overlayer	50	800	50
thickness of FTO	50	800	800

[a]For each parameter, the three columns provide the lower boundary (x_{min}), the upper boundary (x_{max}), and the optimal value (x_{opt}). The theoretical photon-absorption efficiency (fitness) for these optimal parameters is 92.1%.

The absorptance spectrum obtained with the parameters determined by the GA is given in Figure 2. The figure also shows a 2D map of the fitness as a function of the thickness of the 3D-IO nanostructured $MAPbI_3$ perovskite layer and the Spiro-OMeTAD sphere diameter. This map is obtained by an interpolation of the data collected by the GA during optimization. It provides useful insights into the stability of the solution established by the GA. As the map shows, the optimal Spiro-OMeTAD sphere diameter is extremely stable with respect to the thickness of the 3D-IO nanostructured $MAPbI_3$ perovskite layer.

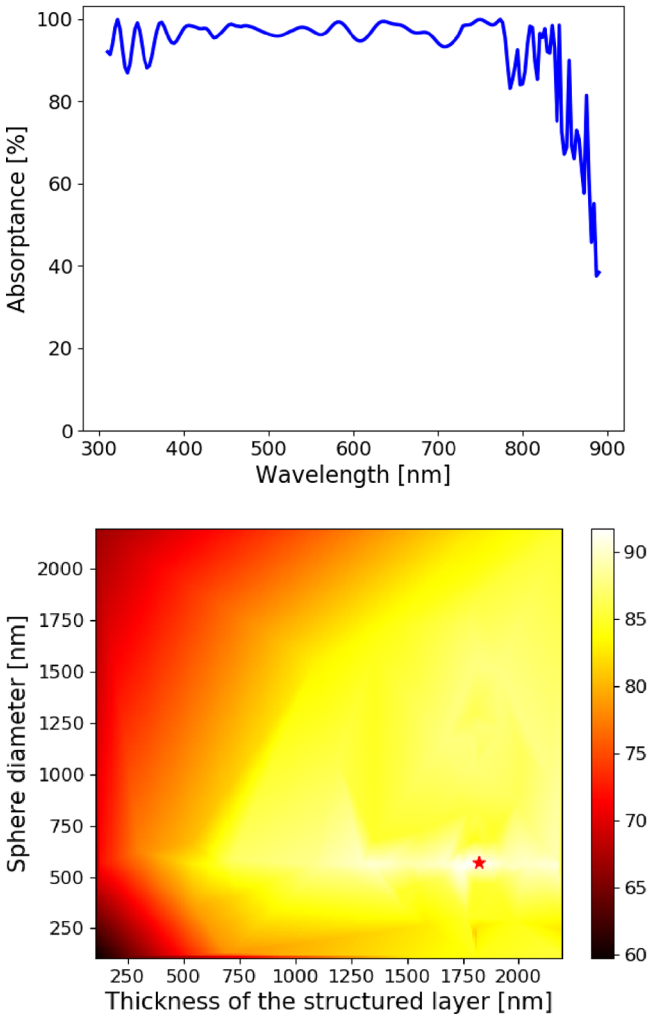

Figure 2. Top: Absorptance spectrum obtained with the optimal parameters of the 3D inverse opal $MAPbI_3$ photonic nanostructure found by the GA. Bottom: Theoretical photon-absorption efficiency as a function of the thickness of the 3D-IO nanostructured $MAPbI_3$ perovskite layer and the Spiro-OMeTAD sphere diameter. The optimum found by the GA is indicated by a red star.

1D maps of the fitness as a function of the thickness of the FTO layer and the thickness of the Spiro-OMeTAD overlayer are also reported in Figure S2 (Supporting Information) in order to assess the stability of the solution established by the GA. The predicted stability is an advantage from a robustness point of view for the experimental realization of the nanostructure.

2.3. Experimental Design of the 3D-IO Nanostructured $MAPbI_3$ Photoanodes. The 3D-IO nanostructured

https://doi.org/10.1021/acsanm.2c03274
ACS Appl. Nano Mater. 2022, 5, 13583−13593

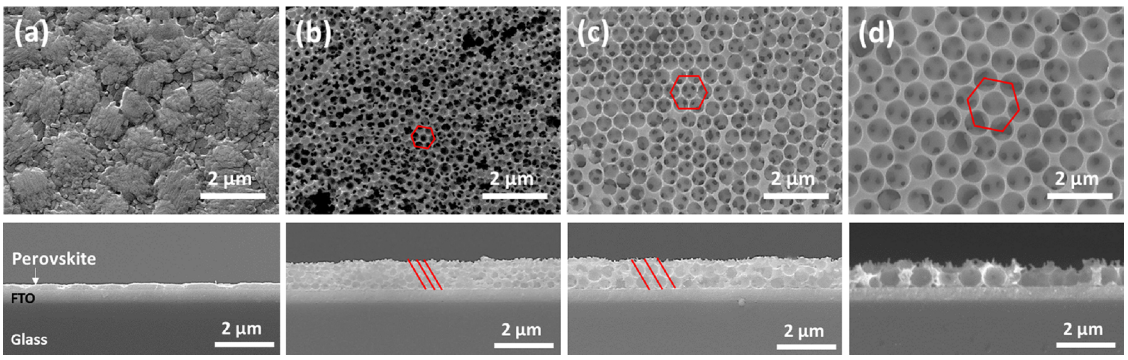

Figure 3. SEM micrographs of (a) $MAPbI_3$-Compact, (b) $MAPbI_3$-PS300, (c) $MAPbI_3$-PS500, and (d) $MAPbI_3$-PS810 perovskite layers. Top-view micrographs (top row) and cross-section micrographs (bottom row). The red marks highlight the periodic organization of the 3D-IO nanostructured perovskite layers.

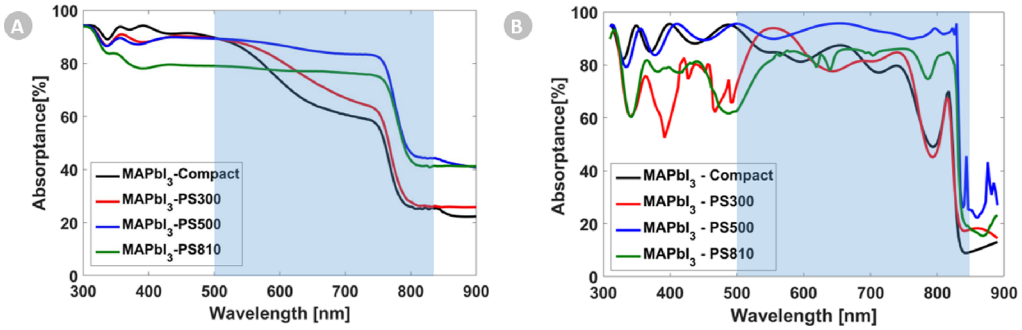

Figure 4. (A) Experimental and (B) simulated UV−VIS−NIR absorptance spectra of the $MAPbI_3$-Compact reference (black line), $MAPbI_3$-PS300 (red line), $MAPbI_3$-PS500 (blue line), and $MAPbI_3$-PS810 (green line) 3D-IO nanostructured perovskite layers.

$MAPbI_3$ perovskite layers are prepared by spin-coating from a 3-step process (detailed description in the Supporting Information, Scheme S1): (a) deposition onto the c-TiO_2/FTO glass substrate of an opal-like template made of polystyrene (PS) nanospheres packed into an fcc lattice; (b) infiltration of the perovskite precursor solution in the interstitial voids between the PS nanospheres to form the perovskite matrix phase; (c) selective removal of the template to obtain the negative of the opal-like PS assembly (= 3D-IO nanostructured $MAPbI_3$ perovskite), with spherical pores embedded into a perovskite matrix.[35,36,38,48,49] Because of the thermal degradation of the perovskite at low temperatures (<150 °C), the PS nanosphere template is removed by chemical washing with toluene. The role of the compact c-TiO_2 layer is to ensure electron selective collection at the photoelectrode and avoid direct contact between FTO and Spiro-OMeTAD HTM.

The thicknesses of the 3D-IO nanostructured $MAPbI_3$ perovskite layer and the pore size range to be experimentally explored in the applied context of solar cells should be the closest to our numerical results presented in Table 1. We therefore investigated different PS nanosphere diameters ranging around the numerical optimum value of 560 nm pore size: 300 nm (PS300), 500 nm (PS500), and 810 nm (PS810). The fine-tuned control of the pore size and pore size dispersion within the perovskite layers is allowed by the large variety of monodisperse PS nanosphere suspensions commercially available. In addition, absorption depth and charge diffusion length for the $MAPbI_3$ formulation studied herein typically range between 100 nm and 1 μm depending on the processing conditions and the final composition, microstructure, and morphology of the deposited layer.[59−64] We therefore chose to reduce the thickness of the experimentally processed 3D-IO nanostructured $MAPbI_3$ perovskite layer to ∼1 μm in spite of the 1.8 μm numerical optimum in order to take these charge transfer limitation aspects into account. It can be seen on Figure 2 that such a reduction still preserves high theoretical photon-absorption efficiency.

As a benchmark, a compact perovskite layer with an equivalent amount of photoactive material is deposited onto a c-TiO_2/FTO glass substrate. The deposition protocol of the compact perovskite benchmark was adapted from ref 57.

2.3.1. Morphological and Structural Characterization. Figure 3 shows the top-view and cross-section SEM micrographs of the different 3D-IO nanostructured $MAPbI_3$ perovskite layers, namely, $MAPbI_3$-PS300, $MAPbI_3$-PS500, and $MAPbI_3$-PS810, respectively, obtained from PS300, PS500, and PS810 templates and the compact benchmark, namely, $MAPbI_3$-Compact.

The different 3D-IO $MAPbI_3$ perovskite layers have similar thicknesses of ∼1.1 μm, leading to similar amounts of photoactive material. They all show a good uniform 3D-IO nanostructuration overall. No contraction of the porous network is observed after PS nanosphere removal by toluene washing, leading to average pore sizes of 300, 500, and 810 nm, similar to the original PS nanosphere diameters. Perovskite wall thicknesses of around 60, 80, and 120 nm average are, respectively, determined from high-magnification SEM micrographs for $MAPbI_3$-PS300, $MAPbI_3$-PS500, and $MAPbI_3$-PS810 perovskite layers. $MAPbI_3$-Compact benchmark presents an island-like structure of 1.0−1.5 μm domain size and an average thickness of 300 nm. Respective thicknesses of around 1.1 μm and 300 nm allow to evidence the photonic nanostructuration effect on the light harvesting properties for a

https://doi.org/10.1021/acsanm.2c03274
ACS Appl. Nano Mater. 2022, 5, 13583−13593

comparable amount of the photoactive material between 3D-IO nanostructured $MAPbI_3$ perovskite layers and the compact reference. Indeed, in the 3D-IO nanostructure, the perovskite fraction should theoretically only represent 26% of the total volume of the close-packed structure, regardless of the pore diameter.[35,65]

From X-ray diffraction (XRD) patterns (Figure S3, Supporting Information), we checked that the pure $MAPbI_3$ perovskite phase composes the 3D-IO perovskite layers. Residual PbI_2 impurity is detected for the $MAPbI_3$-Compact benchmark. PS templates allow to better control $MAPbI_3$ crystallization.[32] From Scherrer analysis, the average $MAPbI_3$ crystallite size is slightly higher for the $MAPbI_3$-Compact benchmark (38 nm) compared to the 3D-IO nanostructured $MAPbI_3$ perovskite layers (33−36 nm). Perovskite containment within the PS nanosphere networks seems to slightly limit the crystallite growth.

2.3.2. Optical Characterization. To assess the light management improvement of the 3D-IO nanostructured $MAPbI_3$ perovskite layers, experimental absorptance spectra (Figure 4A) were measured and compared to simulated data (Figure 4B) for nanostructures without Spiro-OMeTAD infiltration inside the pores and without a gold back reflector/electrode. Simulated absorptance spectra of the different samples were numerically processed from RCWA analysis using the average values of the FTO thickness, the c-TiO_2 thickness, the 3D-IO nanostructured $MAPbI_3$ perovskite layer thickness, and the pore size obtained from the above described morphological and structural analysis.

As previously mentioned, light absorption improvement in the 500− 800 nm wavelength range (highlighted in blue, Figure 4) is especially desired in the case of $MAPbI_3$-based PSCs.[27,28,35] For all samples, a rapid decrease in the absorptance is observed around 800 nm, which is correlated to the electronic band gap of $MAPbI_3$.

The differences in the shape of the experimental and simulated absorption spectra can be attributed to the presence of defects and flaws in experimental structures compared to an ideal theoretical system. Nevertheless, the numerical simulations (Figure 4B) are qualitatively consistent with the experimental spectra (Figure 4A) as we can observe a significant enhancement of the light absorption properties for the $MAPbI_3$-PS500 3D-IO perovskite layer (blue curve). This clearly establishes the benefits of photonic nanostructuration of the perovskite photoactive layers in terms of light management through quasi-guided mode excitation.[40,41] The global absorbance trend can be established as follows from both experimental and numerical spectra: $MAPbI_3$-PS500 > $MAPbI_3$-PS810 ∼ $MAPbI_3$-PS300 ∼ $MAPbI_3$-Compact.

In order to further assess our light management strategy through the 3D-IO photonic nanostructuration of the perovskite layer, different figures of merit were numerically evaluated.[42] As defined in eq 1, the theoretical photon-absorption efficiency η estimates the percentage of incident photons that are absorbed in the whole nanostructure relative to the incident solar spectrum $S(\lambda)$ and the AM1.5G global spectral solar irradiance. Additionally, when comparing η obtained for each of the 3D-IO nanostructured $MAPbI_3$ perovskite layers to the compact benchmark, we can define the photonic gain G_{phot}—resulting from the 3D-IO photonic nanostructuration of the perovskite layers—from eq 2:

$$G_{phot} = \frac{\eta_{struc} - \eta_{compact}}{\eta_{compact}} \times 100 \quad (2)$$

The theoretical photon-absorption efficiency η and the photonic gain G_{phot} of the different 3D-IO nanostructured $MAPbI_3$ perovskite layers and the $MAPbI_3$-Compact benchmark are reported in Table 2.

Table 2. Figures of Merit Used to Numerically Assess Our Light Management Strategy for the 3D-IO Nanostructured $MAPbI_3$ Perovskite Layers, without the Spiro-OMeTAD HTM and Gold Counter Electrode[a]

	η [%]	G_{phot} [%]
$MAPbI_3$-PS300	74.8	−4.5
$MAPbI_3$-PS500	90.9	16.1
$MAPbI_3$-PS810	78.5	0.3
$MAPbI_3$-Compact	78.3	N/A

[a] η is the theoretical photon-absorption efficiency and G_{phot} is the photonic gain relative to the $MAPbI_3$-Compact perovskite layer benchmark.

These figures of merit corroborate the above discussion and prove the positive impact of the photonic nanostructuration on the perovskite layer if the right diameter of spherical pores is chosen. If 300 nm diameter is chosen for the spherical pores, the photonic gain is negative, meaning that the unstructured compact layer is better suited for absorption properties. With 810 nm diameter spherical pores, a very low photonic gain (0.3%) is obtained. On the contrary, the optimal absorption properties of the $MAPbI_3$-PS500 3D-IO perovskite layer presenting 500 nm diameter spherical pores correlates the 560 nm pore size optimum established with the genetic algorithm. The 500 nm diameter spherical pore value allows to accurately position Fano resonance close to $MAPbI_3$ band gap at around 800 nm,[40,41] leading to a G_{phot} as high as 16.1% compared to the $MAPbI_3$-Compact perovskite layer. This enhancement therefore corresponds to 16.1% supplementary generated photoelectrons, if one assumes that each photon generates one electron−hole pair and increases in a way the integrated photon efficiency.

2.4. Photovoltaic Applications: Cell Assembly and Charge Transfer Characterization. The 3D-IO nanostructured $MAPbI_3$ perovskite layers and the compact benchmark were assembled in PSCs to evaluate the effect of the photonic nanostructuration in applied photovoltaic cells (Figure S4, Supporting Information), i.e., Spiro-OMeTAD was infiltrated into the pores and a gold counter electrode/back reflector was deposited. From the $J-V$ curves of our best devices (Figure 5A, data summarized in Table 3), we observed quite low efficiencies for all the PSCs, for both 3D-IO nanostructured and compact perovskite layers. Nevertheless, PCE values slightly improve for the 3D-IO nanostructured $MAPbI_3$ perovskite layers compared to the compact benchmark. The same trend is observed from average values (Table S1, Supporting Information).

Regarding the other PV parameters, the 3D-IO nanostructured $MAPbI_3$ perovskite layers present a higher open-circuit voltage (V_{OC}) and fill factor (FF) compared to the compact benchmark, possibly due to improved charge extraction at the perovskite/Spiro interface.[66] In addition, the $MAPbI_3$_Compact layer contains excess residual PbI_2, which is known to negatively impact V_{OC} and FF due to trap state

https://doi.org/10.1021/acsanm.2c03274
ACS Appl. Nano Mater. 2022, 5, 13583−13593

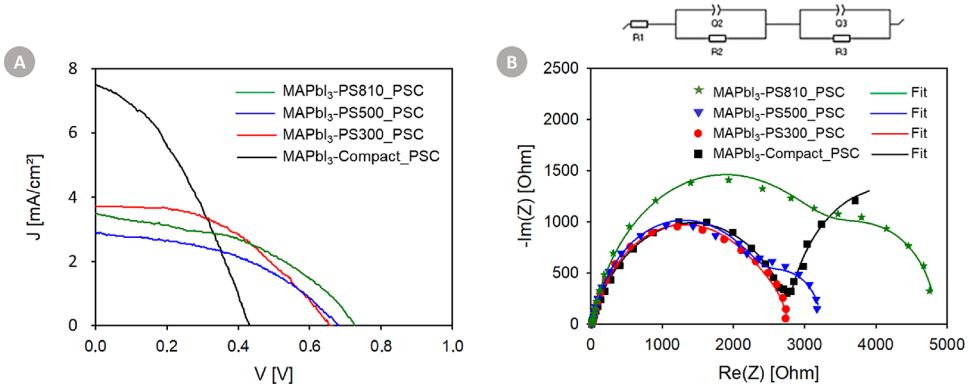

Figure 5. (A) $J-V$ curves and (B) EIS Nyquist plots (equivalent circuit used for data fitting overhead) of our best $MAPbI_3$-Compact_PSC reference (black line), $MAPbI_3$-PS300_PSC (red line), $MAPbI_3$-PS500_PSC (blue line), and $MAPbI_3$-PS810_PSC (green line) assembled devices, with Spiro-OMeTAD HTM and gold back contact.

Table 3. PV Parameters of Open-Circuit Voltage (V_{OC}), Short-Circuit Current Density (J_{sc}), Fill Factor (FF), and Power Conversion Efficiency (PCE) Obtained from $J-V$ Curves Measured on Our Best PSCs Based on Various 3D-IO Nanostructured $MAPbI_3$ Perovskite Photoanodes (Figure 5A)

	V_{OC} [V]	J_{sc} [mA/cm^2]	FF	PCE [%]
$MAPbI_3$-PS300_PSC	0.654	3.6	48	1.8
$MAPbI_3$-PS500_PSC	0.677	2.9	45	1.4
$MAPbI_3$-PS810_PSC	0.723	3.5	44	1.7
$MAPbI_3$-Compact_PSC	0.430	7.5	37	1.1

formation.[67,68] Surprisingly, the 3D-IO nanostructured $MAPbI_3$ perovskite layers show lower short-circuit current densities (J_{sc}) than the compact reference, probably due to the ~1 μm thickness of the nanostructured perovskite layers compared to the 300 nm average thickness for the compact benchmark, therefore leading to increased recombination and lower charge collection at the photoelectrode. This preliminary discussion on the relationships between PV parameters and charge transfer/recombination processes was further investigated and corroborated by electrochemical impedance spectroscopy, as detailed later in the article. Before that, in order to complete the J_{sc} discussion, we should note that its value is particularly low for $MAPbI_3$-PS500_PSC, which is quite contradictory with the light absorption enhancement above reported for the $MAPbI_3$-PS500 3D-IO perovskite layer before device assembly. Therefore, we investigated the light harvesting properties of the 3D-IO nanostructured $MAPbI_3$ perovskite layers when assembled in full devices, considering potential light interaction modification after Spiro-OMeTAD infiltration and gold counter electrode deposition.

The figures of merit of the different 3D-IO nanostructured $MAPbI_3$ perovskite layers and the compact benchmark were then numerically evaluated when assembled in full devices. The theoretical photon-absorption efficiency η and the photonic gain G_{phot} trends are drastically affected by the infiltration of the Spiro-OMeTAD HTM in the perovskite pores, as shown in Table 4. The G_{phot} of 16.1% previously reported for the $MAPbI_3$-PS500 3D-IO perovskite layer is strongly reduced when assembled in the full device stack (2.7%). We observe a similar G_{phot} of around 3% for all the 3D-IO nanostructured $MAPbI_3$ perovskite layers assembled in full devices whatever the pore size, which is slightly higher than for the $MAPbI_3$-Compact_PSC benchmark. An optimal pore size of 500 nm is not evidenced anymore.

Table 4. Figures of Merit Used to Numerically Assess Our Light Management Strategy for the 3D-IO Nanostructured $MAPbI_3$ Perovskite Layers, Assembled in Full Devices with the Spiro-OMeTAD HTM and Gold Counter Electrode[a]

	η [%]	G_{phot} [%]	J_{sc} [mA/cm^2]
$MAPbI_3$-PS300_PSC	89.4	3.1	17.7
$MAPbI_3$-PS500_PSC	89.0	2.7	17.6
$MAPbI_3$-PS810_PSC	89.5	3.2	17.7
$MAPbI_3$-Compact_PSC	86.7	N/A	17.2

[a] η is the theoretical photon-absorption efficiency, G_{phot} is the photonic gain relative to a compact perovskite benchmark, and J_{sc} is the short-circuit current density.

In addition to η and G_{phot}, the short-circuit current density J_{sc}, assuming no electrical losses and neglecting radiative recombination, can also be numerically evaluated by eq 3:

$$J_{sc} = \int_{\lambda_{min}}^{\lambda_{max}} \frac{e\lambda}{hc} S(\lambda)A(\lambda)\mathrm{d}\lambda \quad (3)$$

where e is the elementary electric charge. Calculated values are reported in Table 4.

In accordance with G_{phot} values, a positive effect of the photonic nanostructuration of the $MAPbI_3$-PS500 3D-IO perovskite layer is not anymore observed in the full device compared to $MAPbI_3$-PS300_PSC and $MAPbI_3$-PS810_PSC, which corroborates the $J-V$ curve analysis.

The apparent discrepancy between the 3D-IO nanostructured $MAPbI_3$ perovskite photoanodes, i.e., without Spiro-OMeTAD infiltration inside the pores and without gold back reflector/electrode, and the full devices is tentatively explained as follows.

First of all, from an optical point of view, the addition of the gold back reflector certainly helps structures where light is not tightly confined into the spheres, i.e., transmitted light in the individual 3D-IO nanostructured $MAPbI_3$ perovskite open layers can be bounced back and absorbed within the full devices. It results in globally higher values of η for $MAPbI_3$-Compact_PSC, $MAPbI_3$-PS300_PSC, and $MAPbI_3$-PS810_PSC.

However, we should recall that the absorptance used for calculating η is a global absorptance, i.e., it includes all parts of the solar cells that are able to absorb light. Light absorbed

https://doi.org/10.1021/acsanm.2c03274
ACS Appl. Nano Mater. 2022, 5, 13583−13593

Table 5. Fitted EIS Parameters Obtained from the Data Measured on Our Best PSCs Based on Various 3D-IO Nanostructured $MAPbI_3$ Perovskite Photoanodes Using the Equivalent Circuit Presented in Figure 5B (Inset)

	R_1 [Ω]	Q_2 [10^{-6} F s^{a-1}]	a	R_2 [Ω]	Q_3 [10^{-6} F s^{b-1}]	b	R_3 [Ω]
$MAPbI_3$-PS300_PSC	24.0	1.40	0.824	2518	53.4	0.993	222
$MAPbI_3$-PS500_PSC	18.2	1.10	0.852	2486	38.2	0.976	733
$MAPbI_3$-PS810_PSC	18.0	0.998	0.853	3485	18.0	0.991	1355
$MAPbI_3$-Compact_PSC	11.0	0.424	0.779	2810	59.5	0.968	2776

outside of photoactive regions is referred to as parasitic absorption. Local absorption $A_{loc}(\vec{r}, \omega)$ can help estimating parasitic absorption. Local absorption within a volume V can be written

$$A_{loc}(\vec{r}, \omega) = \frac{\varepsilon_0 \omega}{2P_i} \int_V Im(\varepsilon(\vec{r}, \omega))|E(\vec{r}, \omega)|^2 dV \quad (4)$$

where $\varepsilon(\vec{r}, \omega)$ is the local complex electric permittivity, $E(\vec{r}, \omega)$ is the electric field at position $\vec{r}$, and P_i is the incident power.[69] It is worth reminding here that the 3D-IO nanostructured $MAPbI_3$ PSCs are expected to be composed of 74% of Spiro-OMeTAD HTM and 26% of perovskite photoactive materials. The imaginary part of the electric permittivity of Spiro-OMeTAD is low but non-zero[50] (Figure S5, Supporting Information) and the light-trapping strategy concentrates light inside the Spiro-OMeTAD spheres, i.e., where we have high values for $|E(\vec{r}, \omega)|^2$.[36] Therefore, a considerably higher parasitic absorption can be considered to take place into the full devices compared to the open individual 3D-IO nanostructured $MAPbI_3$ perovskite layers (spheres filled with non-absorbing material, i.e., air), partially explaining the lowered experimental J_{sc} values.

In addition to the parasitic absorption standpoint, the charge transfer properties of the full devices should be discussed as well. As is, 3D-IO nanostructured $MAPbI_3$ perovskite layers could suffer from direct contact between the c-TiO_2 ETL and the Spiro-OMeTAD HTM due to insufficient perovskite coverage, resulting in severe current leakage.[66] In order to prevent direct contact between TiO_2 and Spiro-OMeTAD, Meng *et al.*[33] considered a 200 nm-thick mesoporous TiO_2 layer, filled with $MAPbI_3$, between the c-TiO_2 layer and the nanostructured perovskite layer. To investigate further this potentiality, we have added a 200 nm-thick mesoporous TiO_2 layer in our cell stack without noticing any improvement of the PCE (on the contrary, only 0.5% PCE was obtained for $MAPbI_3$-PS810_PSC with the additional mesoporous TiO_2 layer, Figure S6, Supporting Information). Interestingly, Chen *et al.*[32] reported a design similar to the one reported here (namely, without mesoporous TiO_2 between the c-TiO_2 layer and the nanostructured perovskite layer) and did not observe such a PCE drop. The main reason for that is believed to stand in the lower thickness range of their perovskite photoabsorbing layers, being of ∼500 nm as also reported by Meng *et al.*[33] Nevertheless, in an attempt to design 500 nm-thick nanostructured perovskite layers, we have observed a strong tendency to form cracks all over the film surface, leading to poorly uniform and covering perovskite layers. Such microcracks break the periodicity of the 3D-IO nanostructured perovskite layers and impede subsequent photonic effects. On the contrary, the ∼1 μm-thick 3D-IO nanostructured $MAPbI_3$ perovskite layers lead to less surface cracks and defects and are therefore expected to be much more optimal in terms of light harvesting. Moreover, we should emphasize that the main goal of this study is to materialize the 3D-IO photonically nanostructured $MAPbI_3$ perovskite layers evidenced in our numerical simulations to assess how the optimal photonic nanostructuration of perovskite layers impacts both optical and electronic properties in applied photovoltaic devices. This is why the ∼1 μm thickness range has been investigated. However, the ∼1 μm thickness range of the 3D-IO nanostructured $MAPbI_3$ perovskite layers thus appears to be too detrimental from the electronic point of view as it can further lead to increased recombination and lower charge collection at the photoelectrode, which is consequently detrimental for PCE.

This highlights the fact that the main PCE limitation of the present perovskite nanostructures, selected from numerical simulation, should come from too thick 3D-IO $MAPbI_3$ perovskite layers, impeding accurate charge collection at the photoelectrode. Moreover, charge diffusion length in the $MAPbI_3$ perovskite material is strongly correlated to the size of the crystallites. As our perovskite layers—both compact and 3D-IO nanostructured—present very small ∼40 nm-sized crystallites, the charge diffusion length is expected to be below 200 nm.[61,64]

So, to complete the discussion of charge transfer limitations, electrochemical impedance spectroscopy (EIS) measurements were conducted to probe charge recombination effects, highlighted above as particularly critical toward PCE limitation in our PSCs. Results are presented as Nyquist plots in Figure 5B and fitted according to a 5-element equivalent circuit (inset Figure 5B), including R_1 resistance associated with wires and contacts at high frequencies, $R_2//Q_2$ elements (Q being a constant phase element, modeling an imperfect capacitor) characteristic of the charge transfer at the HTM/perovskite interface at medium frequencies, and $R_3//Q_3$ elements related to charge recombination at low frequencies.[32]

Fitted data (Table 5) show increased electron−hole recombination for the 3D-IO nanostructured perovskite layers compared to the compact benchmark (inversely proportional to R_3).

Within the 3D-IO nanostructured $MAPbI_3$ perovskite layers, the following trend can be established in terms of recombination: $MAPbI_3$-PS300_PSC > $MAPbI_3$-PS500_PSC > $MAPbI_3$-PS810_PSC. During the 3D-IO nanostructured $MAPbI_3$ perovskite layer preparation, PS nanosphere templates have been deposited on c-TiO_2/FTO glass substrates before perovskite infiltration and subsequent PS nanosphere removal to create 3D-IO perovskite porous networks. This has led to uncovered c-TiO_2/FTO glass substrates at the contact points with the PS nanospheres. Proportionally, the lower the PS nanosphere diameter is, the wider the contact points are for the same substrate area. Therefore, more PS300 nanospheres have been coated on the same c-TiO_2/FTO glass surface area than PS500 and PS810 nanospheres, leading to wider direct contact paths between the TiO_2 ETL and the Spiro HTM and subsequently to increased recombination.[66] In addition, from

https://doi.org/10.1021/acsanm.2c03274
ACS Appl. Nano Mater. 2022, 5, 13583−13593

Q_2 values, it can be assumed that more charges accumulate at the perovskite/Spiro-OMeTAD interface for the 3D-IO nanostructured $MAPbI_3$ perovskite layers, which is attributed to a globally limited electron transfer within the ∼1 μm-thick nanostructured perovskite layers. The Q_2 trend seems correlated to the charge separation improvement expected from the perovskite layer nanostructuration and the interface enlargement: $MAPbI_3$-PS300_PSC > $MAPbI_3$-PS500_PSC > $MAPbI_3$-PS810_PSC. Indeed, in the fcc structure, the specific surface (Ss) of the pores is inversely proportional to the pore radius (r), with $Ss = \frac{\pi}{r\sqrt{2}}$ (detailed equations in the Supporting Information). Therefore, at similar thickness, the interface area increases when the pore size decreases. R_2 values also seem to rely on the interface area as charge transfer resistance at the HTM/perovskite interface is higher for $MAPbI_3$-PS810_PSC with the smallest interface. $MAPbI_3$-Compact_PSC could benefit from its unexpected microporosity, enlarging the HTM/perovskite interface.

All in all, the slight global light absorption enhancement promoted by the photonic nanostructuration of the perovskite photoanodes and the improved charge separation at the HTM/perovskite interface overcome limited charge transfer within the ∼1 μm-thick 3D-IO photonically nanostructured $MAPbI_3$ perovskite layers and even slightly boost PCEs compared to the $MAPbI_3$-Compact_PSC benchmark. However, because of the local absorption effects in the Spiro-OMeTAD HTM, we cannot evidence an optimal 3D-IO photonic nanostructure in terms of pore size for the $MAPbI_3$ perovskite photoanodes anymore.

3. CONCLUSIONS

The effect of the 3D inverse opal photonic nanostructuration of the $MAPbI_3$ perovskite photoactive layer in PSCs was numerically instigated and experimentally materialized for the first time.

The benefits of the 3D-IO photonic nanostructuration of the individual perovskite layers on their light absorption properties are strongly affected by the dimensions of the photonic crystal, especially the pore size. An optimum of light absorption is reached for the $MAPbI_3$-PS500 3D-IO perovskite layer, with 500 nm diameter spherical pores, which is in good agreement with the 560 nm pore size optimum established by the genetic algorithm. A photonic absorption enhancement as high as 16.1% is reached for the $MAPbI_3$-PS500 sample compared to the $MAPbI_3$-Compact benchmark.

However, when assembled in full devices, the occurrence of electronics-related countereffects strongly impacts the PSC efficiency, despite the light harvesting improvement provided by the photonic nanostructuration of the materials. Further optimization of the current experimental protocol of PSC assembly should be undertaken to ultimately produce devices with improved PCE values, notably by reducing the 3D-IO nanostructured perovskite layer thickness and by improving perovskite layer coverage in order to avoid direct contact between the c-TiO_2 ETL and the Spiro-OMeTAD HTM. More efficient mixed-cations perovskite formulations, providing improved charge carrier mobility and recombination lifetime, should notably be considered to overcome the charge transfer issue in 1 μm-thick 3D-IO nanostructured perovskite layers.[59,70]

In addition to the highlighted charge transfer limitations in full PSCs, the parasitic absorption present in the other layers, especially in the Spiro-OMeTAD HTM, was found to be non-negligible. This parasitic absorption partly reduces the internal theoretical efficiency and the generation of electron−hole pairs in the assembled devices compared to the individual perovskite layers, leading to a G_{phot} of around 3% for all the 3D-IO nanostructured $MAPbI_3$ perovskite layers without evidencing an optimal pore size anymore. Consequently, the benefits of the 3D-IO photonic nanostructuration of the $MAPbI_3$ perovskite photoanodes on the PCE improvement are quite mitigated at this stage. Using the HTM with reduced parasitic absorption would allow to boost the G_{phot}—as clearly observed for the individual perovskite layers with air in the spherical pores of the 3D-IO perovskite matrix—and subsequently the PCE of the corresponding devices.

In order to go beyond the "exploratory" applied aspect of the present PV results, complementary studies could be carried out to conduct a thorough evaluation of the PSC behavior and efficiency. However, as is, this study already proves the challenge of experimentally materializing numerical calculations/predictions while identifying potential causes of the low efficiencies in the resulting devices. All in all, this work therefore attests to the interest to further develop the nascent field of photonic nanostructuration for enhancing light absorption in advanced photovoltaic materials and devices.

■ ASSOCIATED CONTENT

Supporting Information

The Supporting Information is available free of charge at https://pubs.acs.org/doi/10.1021/acsanm.2c03274.

Additional experimental details, materials, and methods; additional results, including ellipsometric measurements, 1D maps of the GA fitness, X-ray diffractograms, cross-sectional SEM micrographs of the devices, imaginary part of the electric permittivity of the Spiro-OMeTAD HTM, $J-V$ curves, average PV parameters of the devices; and calculation of the specific surface of the pores in the face-centered cubic structure (PDF)

■ AUTHOR INFORMATION

Corresponding Author

Jennifer Dewalque − *Group of Research in Energy and Environment from Materials (GREENMAT), CESAM Research Unit, Chemistry Department, University of Liège, 4000 Liège, Belgium;* orcid.org/0000-0002-8859-9315; Phone: +32 4 366 3438; Email: Jennifer.Dewalque@uliege.be; Fax: +32 4 366 3413

Authors

Nathan Daem − *Group of Research in Energy and Environment from Materials (GREENMAT), CESAM Research Unit, Chemistry Department, University of Liège, 4000 Liège, Belgium*

Alexandre Mayer − *Solid-State Physics Laboratory, Department of Physics, University of Namur, 5000 Namur, Belgium*

Gilles Spronck − *Group of Research in Energy and Environment from Materials (GREENMAT), CESAM Research Unit, Chemistry Department, University of Liège, 4000 Liège, Belgium*

Pierre Colson − *Group of Research in Energy and Environment from Materials (GREENMAT), CESAM*

https://doi.org/10.1021/acsanm.2c03274
ACS Appl. Nano Mater. 2022, 5, 13583−13593

Research Unit, Chemistry Department, University of Liège, 4000 Liège, Belgium; orcid.org/0000-0003-0567-2837

Jerôme Loicq − *Centre Spatial de Liège (CSL), University of Liège, 4031 Liège, Belgium; Space Instrumentation, Faculty of Aerospace Engineering, Delft University of Technology, 2629 HS Delft, The Netherlands*

Catherine Henrist − *Group of Research in Energy and Environment from Materials (GREENMAT), CESAM Research Unit, Chemistry Department, University of Liège, 4000 Liège, Belgium; Center for Applied Research and Education in Microscopy (CAREM), University of Liège, 4000 Liège, Belgium*

Rudi Cloots − *Group of Research in Energy and Environment from Materials (GREENMAT), CESAM Research Unit, Chemistry Department, University of Liège, 4000 Liège, Belgium; Center for Applied Research and Education in Microscopy (CAREM), University of Liège, 4000 Liège, Belgium;* orcid.org/0000-0002-2648-0407

Anthony Maho − *Group of Research in Energy and Environment from Materials (GREENMAT), CESAM Research Unit, Chemistry Department, University of Liège, 4000 Liège, Belgium;* orcid.org/0000-0002-3813-6240

Michaël Lobet − *Solid-State Physics Laboratory, Department of Physics, University of Namur, 5000 Namur, Belgium; Centre Spatial de Liège (CSL), University of Liège, 4031 Liège, Belgium;* orcid.org/0000-0002-4571-0212

Complete contact information is available at: https://pubs.acs.org/10.1021/acsanm.2c03274

Notes

The authors declare no competing financial interest.

■ ACKNOWLEDGMENTS

This research is funded and supported by Fédération Wallonie-Bruxelles (Grant for Concerted Research Actions, "Enhanced Light Scattering for Solar Cells (ELSSOL)" research project, grant agreement ARC 15/19-06) and by Service Public de Wallonie (SOLIDYE_1 Project, Complement FEDER, Grant agreement 1510607). A.M. is funded by Fonds de la Recherche Scientifique de Belgique (F.R.S.-FNRS). Computational resources have been provided by the Consortium des Équipements de Calcul Intensif (CÉCI), funded by Fonds de la Recherche Scientifique de Belgique (F.R.S.-FNRS) under grant agreement 2.5020.11 and by Service Public de Wallonie. Authors would like to acknowledge fellow team members of ULiege (CSL and GREENMAT) and UNamur (LPS) for additional technical and administrative support.

■ REFERENCES

(1) NREL 2022. Best Research-Cell Efficiency Chart. https://www.nrel.gov/pv/cell-efficiency.html.

(2) Moia, D.; Maier, J. Ion Transport, Defect Chemistry, and the Device Physics of Hybrid Perovskite Solar Cells. *ACS Energy Lett.* **2021**, *6*, 1566−1576.

(3) Roy, P.; Kumar Sinha, N.; Tiwari, S.; Khare, A. A Review on Perovskite Solar Cells: Evolution of Architecture, Fabrication Techniques, Commercialization Issues and Status. *Sol. Energy* **2020**, *198*, 665−688.

(4) Mangrulkar, M.; Stevenson, K. J. The Progress of Additive Engineering for $CH_3NH_3PbI_3$ Photo-Active Layer in the Context of Perovskite Solar Cells. *Crystals* **2021**, *11*, 814.

(5) Kojima, A.; Teshima, K.; Shirai, Y.; Miyasaka, T. Organometal Halide Perovskites as Visible-Light Sensitizers for Photovoltaic Cells. *J. Am. Chem. Soc.* **2009**, *131*, 6050−6051.

(6) Zhen, C.; Wu, T.; Chen, R.; Wang, L.; Liu, G.; Cheng, H.-M. Strategies for Modifying TiO_2 Based Electron Transport Layers to Boost Perovskite Solar Cells. *ACS Sustainable Chem. Eng.* **2019**, *7*, 4586−4618.

(7) Liu, J.; Yao, M.; Shen, L. Third Generation Photovoltaic Cells Based on Photonic Crystals. *J. Mater. Chem. C* **2019**, *7*, 3121−3145.

(8) Liu, W.; Ma, H.; Walsh, A. Advance in Photonic Crystal Solar Cells. *Renewable Sustainable Energy Rev.* **2019**, *116*, No. 109436.

(9) Chen, J. D.; Jin, T. Y.; Li, Y. Q.; Tang, J. X. Recent Progress of Light Manipulation Strategies in Organic and Perovskite Solar Cells. *Nanoscale* **2019**, *11*, 18517−18536.

(10) Swatowska, B.; Stapinski, T.; Drabczyk, K.; Panek, P. The Role of Antireflection Coatings in Silicon Solar Cells − The Influence on Their Electrical Parameters. *Opt. Appl.* **2011**, *41*, 487−492.

(11) Raut, H.; Venkatesan, A. G.; Nair, S.; Ramakrishna, S. Anti-Reflective Coatings: A Critical, In-Depth Review. *Energy Environ. Sci.* **2011**, *4*, 3779−3804.

(12) Zambrano, D. F.; Villarroel, R.; Espinoza-González, R.; Carvajal, N.; Rosenkranz, A.; Montaño-Figueroa, A. G.; Arellano-Jiménez, M. J.; Quevedo-Lopez, M.; Valenzuela, P.; Gacitúa, W. Mechanical and Microstructural Properties of Broadband Anti-Reflective TiO_2/SiO_2 Coatings for Photovoltaic Applications Fabricated by Magnetron Sputtering. *Sol. Energy Mater. Sol. Cells* **2021**, *220*, No. 110841.

(13) Basher, M. K.; Hossain, M. K.; Uddin, M. J.; Akand, M. A. R.; Shorowordi, K. M. Effect of Pyramidal Texturization on the Optical Surface Reflectance of Monocrystalline Photovoltaic Silicon Wafers. *Optik* **2018**, *172*, 801−811.

(14) Abdulkadir, A.; Aziz, A. A.; Pakhuruddin, M. Z. Impact of Micro-Texturization on Hybrid Micro/Nano-Textured Surface for Enhanced Broadband Light Absorption in Crystalline Silicon for Application in Photovoltaics. *Mater. Sci. Semicond. Process.* **2020**, *105*, No. 104728.

(15) Huang, Q.; Zhao, J.; Chen, Y.; Wang, J.; Zhao, Y.; Zhang, X.; Hou, G. Plasmonic Modulated Back Reflector for Thin Film Photovoltaics. *Sol. Energy Mater. Sol. Cells* **2021**, *225*, No. 110997.

(16) Lin, Y.-T.; Kumar, G.; Chen, F.-C. Interfacial Plasmonic Effects of Gold Nanoparticle-Decorated Graphene Oxides on the Performance of Perovskite Photovoltaic Devices. *Sol. Energy* **2020**, *211*, 822−830.

(17) Ho, W.-J.; Feng, S.-K.; Liu, J.-J.; Yang, Y.-C.; Ho, C.-H. Improving Photovoltaic Performance of Silicon Solar Cells Using a Combination of Plasmonic and Luminescent Downshifting Effects. *Appl. Surf. Sci.* **2018**, *439*, 868−875.

(18) Mustafa, M. N.; Sulaiman, Y. Review on the Effect of Compact Layers and Light Scattering Layers on the Enhancement of Dye-Sensitized Solar Cells. *Sol. Energy* **2021**, *215*, 26−43.

(19) Bhattacharya, S.; John, S. Photonic Crystal Light Trapping: Beyond 30% Conversion Efficiency for Silicon Photovoltaics. *APL Photonics* **2020**, *5*, No. 020902.

(20) Bermel, P.; Luo, C.; Zeng, L.; Kimerling, L. C.; Joannopoulos, J. D. Improving Thin-Film Crystalline Silicon Solar Cell Efficiencies with Photonic Crystals. *Opt. Express* **2007**, *15*, 16986−17000.

(21) Gomard, G.; Peretti, R.; Drouard, E.; Meng, X.; Seassal, C. Photonic Crystals and Optical Mode Engineering for Thin Film Photovoltaics. *Opt. Express* **2013**, *21*, A515−A527.

(22) Üpping, J.; Bielawny, A.; Wehrspohn, R.; Beckers, T.; Carius, R.; Rau, U.; Fahr, S.; Rockstuhl, C.; Lederer, F.; Kroll, M.; Pertsch, T.; Steidl, L.; Zentel, R. Three-Dimensional Photonic Crystal Intermediate Reflectors for Enhanced Light-Trapping in Tandem Solar Cells. *Adv. Mater.* **2011**, *23*, 3896−3900.

(23) Limonov, M. F.; Rybin, M. V.; Poddubny, A. N.; Kivshar, Y. S. Fano Resonances in Photonics. *Nat. Photonics* **2017**, *11*, 543−554.

(24) Joannopoulos, J. D.; Johnson, S. G.; Winn, J. N.; Meade, R. D. *Photonic Crystals: Molding the Flow of Light*. Princeton University Press: Princeton, 2008.

(25) Yablonovitch, E. Inhibited Spontaneous Emission in Solid-State Physics and Electronics. *Phys. Rev. Lett.* **1987**, *58*, 2059−2062.

(26) John, S. Strong Localization of Photons in Certain Disordered Dielectric Superlattices. *Phys. Rev. Lett.* **1987**, *58*, 2486−2489.
(27) Lee, M. M.; Teuscher, J.; Miyasaka, T.; Murakami, T. N.; Snaith, H. J. Efficient Hybrid Solar Cells Based on Meso-Superstructured Organometal Halide Perovskites. *Science* **2012**, *338*, 643−647.
(28) Im, J.-H.; Lee, C.-R.; Lee, J.-W.; Park, S.-W.; Park, N.-G. 6.5% Efficient Perovskite Quantum-Dot-Sensitized Solar Cell. *Nanoscale* **2011**, *3*, 4088−4093.
(29) Ramos, F. J.; Oliva-Ramírez, M.; Nazeeruddin, M. K.; Graetzel, M.; González-Elipe, A. R.; Ahmad, S. Light Management: Porous 1-Dimensional Nanocolumnar Structures as Effective Photonic Crystals for Perovskite Solar Cells. *J. Mater. Chem. A* **2016**, *4*, 4962−4970.
(30) Zhang, L.; Hörantner, M. T.; Zhang, W.; Yan, Q.; Snaith, H. J. Near-Neutral-Colored Semitransparent Perovskite Films Using a Combination of Colloidal Self-Assembly and Plasma Etching. *Sol. Energy Mater. Sol. Cells* **2017**, *160*, 193−202.
(31) Hörantner, M. T.; Zhang, W.; Saliba, M.; Wojciechowski, K.; Snaith, H. J. Templated Microstructural Growth of Perovskite Thin Films via Colloidal Monolayer Lithography. *Energy Environ. Sci.* **2015**, *8*, 2041−2047.
(32) Chen, B.-X.; Rao, H.-S.; Chen, H.-Y.; Li, W.-G.; Kuang, D.-B.; Su, C.-Y. Ordered Macroporous $CH_3NH_3PbI_3$ Perovskite Semitransparent Film for High-Performance Solar Cells. *J. Mater. Chem. A* **2016**, *4*, 15662−15669.
(33) Meng, K.; Gao, S.; Wu, L.; Wang, G.; Liu, X.; Chen, G.; Liu, Z.; Chen, G. Two-Dimensional Organic-Inorganic Hybrid Perovskite Photonic Films. *Nano Lett.* **2016**, *16*, 4166−4173.
(34) Kang, S. M.; Jang, S.; Lee, J.-K.; Yoon, J.; Yoo, D.-E.; Lee, J.-W.; Choi, M.; Park, N.-G. Moth-Eye TiO_2 Layer for Improving Light Harvesting Efficiency in Perovskite Solar Cells. *Small* **2016**, *12*, 2443−2449.
(35) Maho, A.; Lobet, M.; Daem, N.; Piron, P.; Spronck, G.; Loicq, J.; Cloots, R.; Colson, P.; Henrist, C.; Dewalque, J. Photonic Structuration of Hybrid Inverse-Opal TiO_2-Perovskite Layers for Enhanced Light Absorption in Solar Cells. *ACS Appl. Energy Mater.* **2021**, *4*, 1108−1119.
(36) Chen, K.; Tüysüz, H. Morphology-Controlled Synthesis of Organometal Halide Perovskite Inverse Opals. *Angew. Chem., Int. Ed.* **2015**, *54*, 13806−13810.
(37) Schünemann, S.; Chen, K.; Brittman, S.; Garnett, E.; Tüysüz, H. Preparation of Organometal Halide Perovskite Photonic Crystal Films for Potential Optoelectronic Applications. *ACS Appl. Mater. Interfaces* **2016**, *8*, 25489−25495.
(38) Schünemann, S.; Brittman, S.; Chen, K.; Garnett, E. C.; Tüysüz, H. Halide Perovskite 3D Photonic Crystals for Distributed Feedback Lasers. *ACS Photonics* **2017**, *4*, 2522−2528.
(39) Dokkhan, C.; Mokhtar, M. Z.; Chen, Q.; Saunders, B. R.; Hodson, N. W.; Hamilton, B. Using Microgels to Control the Morphology and Optoelectronic Properties of Hybrid Organic−Inorganic Perovskite Films. *Phys. Chem. Chem. Phys.* **2018**, *20*, 27959−27969.
(40) Lobet, M.; Piron, P.; Dewalque, J.; Maho, A.; Deparis, O.; Henrist, C.; Loicq, J. Efficiency Enhancement of Perovskite Solar Cells Based on Opal-like Photonic Crystals. *Opt. Express* **2019**, *27*, 32308−32322.
(41) Lobet, M.; Mayer, A.; Maho, A.; Piron, P.; Dewalque, J.; Henrist, C.; Loicq, J. Opal-Like Photonic Structuring of Perovskite Solar Cells Using a Genetic Algorithm Approach. *Appl. Sci.* **2020**, *10*, 1783.
(42) Schmager, R.; Gomard, G.; Richards, B. S.; Paetzold, U. W. Nanophotonic Perovskite Layers for Enhanced Current Generation and Mitigation of Lead in Perovskite Solar Cells. *Sol. Energy Mater. Sol. Cells* **2019**, *192*, 65−71.
(43) Chen, X.; Yang, S.; Zheng, Y. C.; Chen, Y.; Hou, Y.; Yang, X. H.; Yang, H. G. Multifunctional Inverse Opal-Like TiO_2 Electron Transport Layer for Efficient Hybrid Perovskite Solar Cells. *Adv. Sci.* **2015**, *2*, 1500105.
(44) Ha, S.-J.; Heo, J. H.; Im, S. H.; Moon, J. H. Mesoscopic $CH_3NH_3PbI_3$ Perovskite Solar Cells Using TiO_2 Inverse Opal Electron-Conducting Scaffolds. *J. Mater. Chem. A* **2017**, *5*, 1972−1977.
(45) Sun, S.; Xie, Z.; Qin, G.; Xiao, L. Light Trapping Nano Structures with over 30% Enhancement in Perovskite Solar Cells. *Org. Electron.* **2019**, *75*, No. 105385.
(46) Gupta, N. Absorption Enhancement in Hole Interface Layer Free Perovskite Solar Cells Using Periodic Photonic Nanostructures. *Opt. Laser Technol.* **2019**, *115*, 20−31.
(47) Du, Q. G.; Shen, G.; John, S. Light-Trapping in Perovskite Solar Cells. *AIP Adv.* **2016**, *6*, No. 065002.
(48) Fang, J.; Xuan, Y.; Li, Q. Preparation of Polystyrene Spheres in Different Particle Sizes and Assembly of the PS Colloidal Crystals. *Sci. China Technol. Sci.* **2010**, *53*, 3088−3093.
(49) Wijnhoven, J.; Vos, W. Preparation of Photonic Crystals Made of Air Spheres in Titania. *Science* **1998**, *281*, 802−804.
(50) Mayer, A.; Lobet, M. UV to Near-Infrared Broadband Pyramidal Absorbers via a Genetic Algorithm Optimization Approach. *Proc. SPIE* **2018**, *10671*, 1067127.
(51) Mayer, A.; Bi, H.; Griesse-Nascimento, S.; Hackens, B.; Loicq, J.; Mazur, E.; Deparis, O.; Lobet, M. Genetic-Algorithm-Aided Ultra-Broadband Perfect Absorbers Using Plasmonic Metamaterials. *Opt. Express* **2022**, *30*, 1167−1181.
(52) Moharam, M.; Gaylord, T. Rigorous Coupled-Wave Analysis of Planar-Grating Diffraction. *J. Opt. Soc. Am.* **1981**, *71*, 811−818.
(53) Lobet, M.; Lard, M.; Sarrazin, M.; Deparis, O.; Henrard, L. Plasmon Hybridization in Pyramidal Metamaterials: A Route towards Ultra-Broadband Absorption. *Opt. Express* **2014**, *22*, 12678−12690.
(54) Rubin, M. Optical Properties of Soda Lime Silica Glasses. *Sol. Energy Mater.* **1985**, *12*, 275−288.
(55) Ball, J. M.; Stranks, S. D.; Hörantner, M. T.; Hüttner, S.; Zhang, W.; Crossland, E. J. W.; Ramirez, I.; Riede, M.; Johnston, M. B.; Friend, R. H.; Snaith, H. J. Optical Properties and Limiting Photocurrent of Thin-Film Perovskite Solar Cells. *Energy Environ. Sci.* **2015**, *8*, 602−609.
(56) Olmon, R. L.; Slovick, B.; Johnson, T. W.; Shelton, D.; Oh, S.-H.; Boreman, G. D.; Raschke, M. B. Optical Dielectric Function of Gold. *Phys. Rev. B* **2012**, *86*, No. 235147.
(57) Saliba, M.; Correa-Baena, J.-P.; Wolff, C. M.; Stolterfoht, M.; Phung, N.; Albrecht, S.; Neher, D.; Abate, A. How to Make over 20% Efficient Perovskite Solar Cells in Regular (n−i−p) and Inverted (p−i−n) Architectures. *Chem. Mater.* **2018**, *30*, 4193−4201.
(58) Hussain, I.; Tran, H. P.; Jaksik, J.; Moore, J.; Islam, N.; Uddin, M. J. Functional Materials, Device Architecture, and Flexibility of Perovskite Solar Cell. *Emergent Mater.* **2018**, *1*, 133−154.
(59) Stranks, S. D.; Eperon, G. E.; Grancini, G.; Menelaou, C.; Alcocer, M. J. P.; Leijtens, T.; Herz, L. M.; Petrozza, A. M.; Snaith, H. J. Electron-Hole Diffusion Lengths Exceeding 1 Micrometer in an Organometal Trihalide Perovskite Absorber. *Science* **2013**, *342*, 341−344.
(60) Momblona, C.; Malinkiewicz, O.; Roldán-Carmona, C.; Soriano, A.; Gil-Escrig, L.; Bandiello, E.; Scheepers, M.; Edri, E.; Bolink, H. J. Efficient Methylammonium Lead Iodide Perovskite Solar Cells with Active Layers from 300 to 900 nm. *APL Mater.* **2014**, *2*, No. 081504.
(61) Adhyaksa, G. W. P.; Veldhuizen, L. W.; Kuang, Y.; Brittman, S.; Schropp, R. E. I.; Garnett, E. C. Carrier Diffusion Lengths in Hybrid Perovskites: Processing, Composition, Aging, and Surface Passivation Effects. *Chem. Mater.* **2016**, *28*, 5259−5263.
(62) Wang, H. Y.; Hao, M. Y.; Han, J.; Yu, M.; Qin, Y.; Zhang, P.; Guo, Z. X.; Ai, X. C.; Zhang, J. P. Adverse Effects of Excess Residual PbI_2 on Photovoltaic Performance, Charge Separation, and Trap-State Properties in Mesoporous Structured Perovskite Solar Cells. *Chem. − Eur. J.* **2017**, *23*, 3986−3992.
(63) Nguyen, V. H.; Hoang, T. K. A.; Kurokawa, Y.; Usami, N. The Impact of Highly Excessive PbI_2 on the Correlation of $MAPbI_3$ Perovskite Morphology and Carrier Lifetimes. *J. Mater. Chem. C* **2020**, *8*, 14481−14489.

https://doi.org/10.1021/acsanm.2c03274
ACS Appl. Nano Mater. 2022, 5, 13583−13593

(64) Shargaieva, O.; Lang, F.; Rappich, J.; Dittrich, T.; Klaus, M.; Meixner, M.; Genzel, C.; Nickel, N. The Influence of the Grain Size on the Properties of $CH_3NH_3PbI_3$ Thin Films. *ACS Appl. Mater. Interfaces* **2017**, *9*, 38428−38435.
(65) Henrist, C.; Dewalque, J.; Cloots, R.; Vertruyen, B.; Jonlet, J.; Colson, P. Hierarchical Porous TiO_2 Thin Films by Soft and Dual Templating. *Thin Solid Films* **2013**, *539*, 188−193.
(66) Huang, F.; Pascoe, A. R.; Wu, W. Q.; Ku, Z.; Peng, Y.; Zhong, J.; Caruso, R. A.; Cheng, Y. B. Effect of the Microstructure of the Functional Layers on the Efficiency of Perovskite Solar Cells. *Adv. Mater.* **2017**, *29*, 1601715.
(67) Roose, B.; Dey, K.; Chiang, Y. H.; Friend, R. H.; Stranks, S. D. Critical Assessment of the Use of Excess Lead Iodide in Lead Halide Perovskite Solar Cells. *J. Phys. Chem. Lett.* **2020**, *11*, 6505−6512.
(68) Jacobsson, T. J.; Correa-Baena, J.-P.; Halvani Anaraki, E.; Philippe, B.; Stranks, S. D.; Bouduban, M. E. F.; Tress, W.; Schenk, K.; Teuscher, J.; Moser, J.-E.; Rensmo, H.; Hagfeldt, A. Unreacted PbI_2 as a Double-Edged Sword for Enhancing the Performance of Perovskite Solar Cells. *J. Am. Chem. Soc.* **2016**, *138*, 10331−10343.
(69) Brenner, K.-H. Aspects for Calculating Local Absorption with the Rigorous Coupled-Wave Method. *Opt. Express* **2010**, *18*, 10369−10376.
(70) Rehman, W.; McMeekin, D. P.; Patel, J. B.; Milot, R. L.; Johnston, M. B.; Snaith, H. J.; Herz, L. M. Photovoltaic Mixed-Cation Lead Mixed-Halide Perovskites: Links between Crystallinity, Photo-Stability and Electronic Properties. *Energy Environ. Sci.* **2017**, *10*, 361−369.

https://doi.org/10.1021/acsanm.2c03274
ACS Appl. Nano Mater. 2022, 5, 13583−13593